JOURNAL OF Materials CHEMISTRY

Sol–gel synthesis and electrical properties of $(ZrO_2)_{0.85}(REO_{1.5})_{0.15}$ (RE = Sc, Y) solid solutions

Yawen Zhang, Yu Yang, Shujian Tian, Chunsheng Liao and Chunhua Yan*

State Key Lab of Rare Earth Materials Chemistry and Applications & PKU-HKU Joint Lab on Rare Earth Materials and Bioinorganic Chemistry, Peking University, Beijing 100871, China. E-mail: chyan@chem.pku.edu.cn

Received 30th July 2001, Accepted 25th October 2001
First published as an Advance Article on the web 18th December 2001

$(ZrO_2)_{0.85}(REO_{1.5})_{0.15}$ (RE = Sc, Y) solid solutions in a pure cubic fluorite structure with uniform grain sizes ranging from nanometers to microns have been synthesized by a Pechini-type sol–gel method, using weakly cross-linked polymers. Metal nitrates, poly(ethylene glycol) and carboxylic acids such as acetic acid and formic acid, have been utilized to make the homogeneous polymer precursor solutions. Owing to its stronger acidity and coordinating capability, formic acid seems more effective in preventing the metal hydroxides segregating from the precursor solutions than does acetic acid during the gel formation. The Sc-doped zirconia derived from the formic acid-containing gel could achieve good-crystallization in the pure cubic phase at sintering temperatures as low as 1000 °C. Gel-calcined powders at 800 °C are mesoporous nanoparticles with narrow size distribution, and show a cubic structure attributed to the crystallite size effect. The polymeric precursor compositions display considerable impact on the gel formation, powder reactivity, crystallization of the sintered body, and finally the ionic conductivity of the grain boundary. However, the bulk ionic conductivity is dependent on the sintering temperature and variety of the dopants, rather than on the precursor compositions. Both the bulk and grain boundary conductivities increase when the sintering temperature/density are raised.

Introduction

Close investigation of the relationship between ceramic microstructures and their preparative methods has been one current focus in the disciplines of chemistry and materials science, because the microstructures ultimately determine the properties of the materials.[1–3] A rational synthesis route not only enables the microstructures to be readily controlled from micron to nanometer regime, but also enables the properties to be smoothly tailored.

Formerly, much attention has been paid to the electrical properties of yttria- or scandia-stabilized zirconia (YSZ, ScSZ), as the promising candidate electrolytes of solid oxide fuel cells (SOFCs). However, the impact of the synthesis route on the ceramic microstructures and properties has been inadequately explored.[4–6] More recently, the electrical properties of the nanostructured ionic conductors such as $(ZrO_2)_{0.85}(YO_{1.5})_{0.15}$ and $(ZrO_2)_{0.85}(ScO_{1.5})_{0.15}$ have been attractive research topics.[7–10] The clarification of ionic conduction in the bulk stabilized ZrO_2 requires the preparation of desirable microstructures with controlled grain size and size distribution, pure grain boundaries and enhanced chemical homogeneity by various fabrication techniques. Therefore, it is of great necessity to elucidate the relationship between the performance of the ceramic electrolytes and the synthesis route.

Generally, zirconia-based ceramics can be prepared by various methods such as solid state reaction,[11] co-precipitation,[12] thermo-decomposition of complex precursors[13] and the sol–gel route.[14,15] Among them, the sol–gel method has the ability to make multicomponent oxide powders with superior homogeneity. For the various sol–gel methods, the polymeric precursor route is advantageous over the Pechini-type *in-situ* polymerizable complex approach and the metaloxane polymer process for its simplicity, lower cost of organics, much lower toxicity, greater versatility and improved sinterability.[16]

In the polymeric precursor route, water-soluble polymers such as poly(vinyl alcohol) (PVA), poly(acrylic acid) (PAA), poly(ethyleneimine) (PEI) and poly(ethlene glycol) (PEG) are often used. The cross-linking between the metal ions and the polymers seems to play a crucial role in governing the efficiency of this approach.[16] On the other hand, the mobility of cations incorporated in the polymer matrix *via* coordination bonds and/or intermolecular interactions is likely to correlate with the segregation of metal ions throughout the resulting gel. However, there is further need for the use of characterization techniques to monitor changes in homogeneity at different stages of this method.

Mizutani *et al.* repeatedly synthesized a ScSZ polycrystalline material in a pure cubic fluorite structure by the polymer precursor method using the weakly cross-linked polymer PEG, but gave no detailed characterization regarding the synthesis process.[15] By a simple Pechini-type sol–gel spin coating method, employing a precursor solution composed of PEG and metal nitrates, we recently prepared a series of rare earth-stabilized zirconia thin films (dense, crack-free and uniform) on a single crystal Si substrate, and observed an enhanced ionic conduction in $(ZrO_2)_{0.85}(REO_{1.5})_{0.15}$ (RE = Sc,Y) films.[9] The objective of this study is to reveal how the Pechini-type sol–gel route affects the microstructure and electrical properties of the $(ZrO_2)_{0.85}(REO_{1.5})_{0.15}$ (RE = Sc, Y) solid solutions. In this paper, the influences of polymeric precursors consisting of metal nitrates, PEG, and acetic acid (or formic acid) on the gel characteristics, calcination and sintering behaviors, and the ionic conductivity are presented.

Experimental

Sol–gel preparation

$ZrO(NO_3)_2$ (AR, 17 mmol), $Sc(NO_3)_3$ (AR, 3 mmol) [or $Y(NO_3)_3$], acetic acid (20–180 mmol) (or formic acid), 1–6 g of PEG (CP grade, molecular weight 20 000) were taken to make a given stock solution (50 mL) in a flask (100 mL). After being refluxed at 120 °C for 1 h in an oil bath, the color of the

DOI: 10.1039/b106876h

Table 1 Nomenclature and polymeric precursor compositions of the samples

Sample	C_M/mol L^{-1}	C_{PEG}/mg mL^{-1}	C_A/mol L^{-1}	C_F/ mol L^{-1}
SA1	0.4	20	1.2	
SA2	0.4	20	2.4	
SA3	0.4	50	2.4	
SF1	0.4	50		1.2
SF2	0.4	50		2.4
YA1	0.4	20	1.2	

stock solution gradually became yellowish, due to the fact that HNO_3 decomposed with liberation of NO_x gases. After a total reflux period of 24 h, a transparent polymer precursor solution had been formed. Through evaporation on an electric oven in open air, the precursor became viscous, while further decomposition of HNO_3 occurred. The viscous liquid was then kept drying at 110 °C until a yellow or white sponge-like gel was yielded.

The dried gel was pulverized using an agate pestle and mortar, and then calcined at 800 °C for 10 h in a muffle furnace to remove the organic impurities. For preparing dense specimens, the gel-calcined powders (0.15–0.4 g) were ground for 15 min using an agate pestle and mortar, then uniaxially pressed into pellet specimens with a diameter of 6 mm under 12 MPa pressure. Finally, the specimens were sintered under still air at various temperatures (1000–1400 °C) for 24 h.

The nomenclature and polymeric precursor compositions of some samples are listed in Table 1, where S, Y, A and F denote scandium, yttrium, acetic acid and formic acid, respectively; C_M, C_{PEG}, C_A and C_F are the concentrations of metal ions, PEG, acetic acid and formic acid, respectively.

Characterization methods

Elemental analysis of C, H and N was performed with the Carlo Erba 1102 elemental analyzer. FTIR spectra were measured by microscopic IR, using a Nicolet Magna 750 FTIR spectrometer in the ranges 400–4000 cm^{-1} and 50–650 cm^{-1}. Thermo-gravimetry and differential thermal analysis (TG–DTA) curves were recorded with a thermal analyzer (Du Pont 2100) in air at a heating rate of 10 °C min^{-1}, using α-Al_2O_3 as a reference. The crystal structures were identified by a powder X-ray diffractometer (XRD, Rigaku D/max-2000), employing Cu-Kα radiation (λ = 1.5408 Å). With the software 'LAPOD' of least-squares refinement of cell dimensions from powder data by Cohen's Method,[17,18] the lattice parameters were calculated. The average grain size D was estimated according to the Scherrer equation,[19]

$$D = 0.90\lambda/\beta\cos\theta$$

where, θ is the diffraction angle of the (111) peak, β is the full width at half maximum (FWHM) of the (111) peak (in radians), which is calibrated from high purity silicon. The BET specific surface area S_{BET} and pore volume (V_p) distribution were measured by nitrogen physisorption at 77.5 K, using an ASAP 2010 analyzer (Micromeritics Co. Ltd.). The pore size distribution was calculated from the adsorption branch of the isotherms, based on the BJH method.[20] The BJH pore diameter (r_p) was calculated as $4V_p/S_{BJH}$. Sample microstructures (in selected cases, surfaces were gold-coated) were determined by scanning electron microscopy (SEM, AMARY 1910FE).

Electrical property measurements

The electrical properties of the dense specimens were determined in air by AC two-probe measurements on a frequency response analyzer (HP-4192A LF, 200 Hz–12 MHz).[21] The impedance data points were collected with a temperature interval of 60 °C on cooling down over the temperature range of 950–350 °C. Two Pt lead wire electrodes were adhered to two terminal surfaces of the specimen with Pt paste, which was fired at 950 °C for 30 min to remove the polymeric components. The ionic conductivity was calculated from the interceptions of the observed semicircle on the real axis of the Cole–Cole plot.

Results and discussion

Characterization of the gel

TG analysis of the gels with a fixed content of PEG showed that the weight loss percentage increased with increasing molar ratio of acetic acid to metal ions from 1 : 1 to 6 : 1 in the precursors, but that it varied little with raising the ratio from 6 : 1 to 9 : 1. This observation hints that excessive acetic acid (bp: 117.9 °C) would be driven out by evaporation and drying during the gel formation. Thus, the molar ratio of acetic acid to metal ions below 6 : 1 should be the most favored for gel preparation.

In the polymer precursor route, for avoiding the segregation of metal ions throughout gel formation, the metal ions are coordinated by the chelating ligand and uniformly incorporated into the polymer matrix *via* coordination bonds and intermolecular interactions of Van der Waals and/or hydrogen bonding. Experimentally, refluxing of the stock solution resulted in coordination between the metal ions and the acetic acid (or formic acid), and partial breakup of the nitric acid. Fig. 1 shows the IR spectra of the **SF1** precursor solution before and after refluxing, and far IR spectra of the **SA1** and **SF1** precursor solutions after refluxing. In the presence of excessive carboxylic acid, the vibration frequency and intensity related to the free carboxylic acid and carbonyl group display few changes after refluxing. However, the nitrate content is greatly reduced, as indicated by the sharp drop of the intensity of the peak at *ca.* 1375 cm^{-1} [Fig. 1(a)]. This peak is associated with uncoordinated nitrate ions.[22] After refluxing, the coordination between the metal ions and the carboxylic group was identified by the emergence of the peak lying within *ca.* 450–550 cm^{-1} in the far IR spectra [Fig. 1(b)]. The peak of *ca.* 250–450 cm^{-1} can be ascribed to ν_{M-O} of the ZrO^{2+} cations. Previously, the zirconium species in aqueous solution was

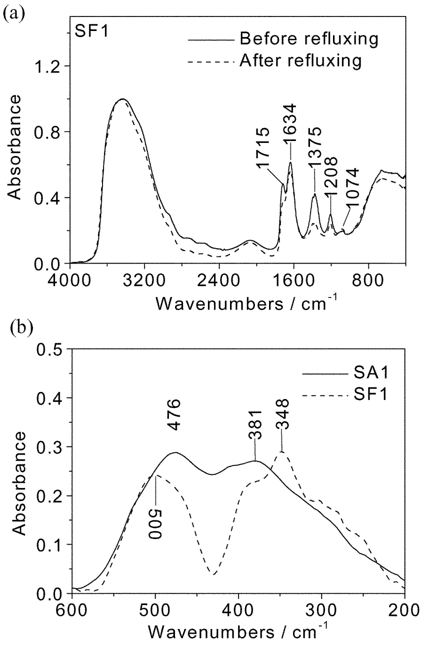

Fig. 1 IR spectra of the **SF1** precursor solution before and after refluxing (a), and far-IR spectra of the **SA1** and **SF1** precursor solutions after refluxing (b).

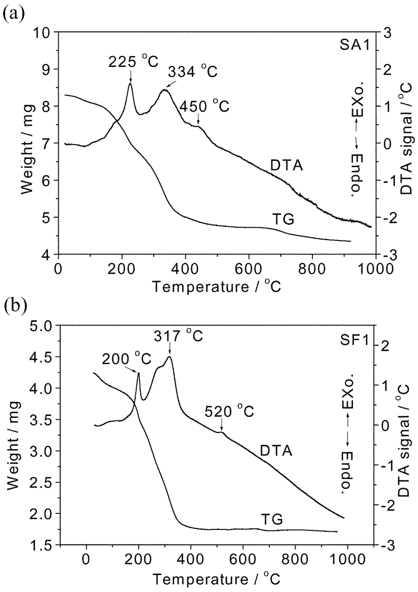

Fig. 2 Combined TG–DTA run of the **SA1** (a) and **SF1** (b) gels.

reported to exist in the form of diacetatozirconic acid by Geiculescu and Spencer.[23]

Fig. 2 typically exhibits a combined TG–DTA run of the **SA1** and **SF1** gels. The curves show that **SA1** and **SF1** take on a similar decomposition process, which can be roughly divided into three steps. The first is the breakdown of the residual nitric acid at *ca.* 200 °C, giving a medium exothermic peak. Kwon *et al.* reported that nitrate decomposed in the temperature range of 180–260 °C in preparing the lithium aluminate *via* a polymeric precursor route.[24] The second step is the cleavage of the organic components composed of PEG, free carboxylic acid and the corresponding complexes in the temperature range of 270–390 °C, accompanied by a very strong exothermic peak. We, however, observed that PEG broke down in the temperature range of 250–350 °C.[6] Huang and Goodenough found that the decomposition of CH_3COO^- ligands and the corresponding complexes generated exothermic peaks at 280 and 330 °C, respectively, when they used metal acetate and nitrate as the starting materials to prepare Sr- and Mg-doped $LaGaO_3$ ultrafine powders by the sol–gel process.[25] Lastly, a very weak exothermic effect along with a small weight loss was noticed in the temperature range of *ca.* 450–480 °C for **SA1** and *ca.* 480–520 °C for **SF1**, respectively. Such a small exothermal effect might be produced by the transition from an amorphous to cubic structure during the gel decomposition.[23,26]

Calcination behavior

By the elemental analysis, the total amount of the remnant organic substances in the powders derived from the gel calcined at 800 °C was determined to be below 0.1%, which is low enough to satisfy with the basic requirement of pure ceramic electrolytes. Fig. 3 displays the XRD patterns of **SA1**, **SA2**, **SA3**, **SF1** and **YA1** samples in the 2θ range of 20–90°, and the scale-enlarged profile of **SA1** over 70–80° (inset). The broadening of the diffraction peaks clearly reveals the nanocrystal formation. **SA3**, **SF1** and **YA1** are well-crystallized in a pure cubic fluorite structure. **SA1** and **SA2** comprise predominately cubic and trace monoclinic structures, possibly caused by the chemical inhomogeneity of the microdomain, correlative with the segregation of some metal ions into the sol or colloid during gel formation. Yashima *et al.* report that the formation of the sol or colloid could lead to compositional inhomogeneity and thus the phase splitting in their preparation of $(ZrO_2)_{1-x}(CeO_2)_x$ ($x = 0.2$, 0.5) solid solutions by the Pechini method.[27] In fact, the nanoparticles with a pure or predominately cubic phase can be interpreted in terms of the crystallite size effect, as was found in the nanostructured zirconia systems.[28,29] The larger surface energies of the smaller grain sizes are liable to bring on the higher energy phase (cubic or tetragonal).

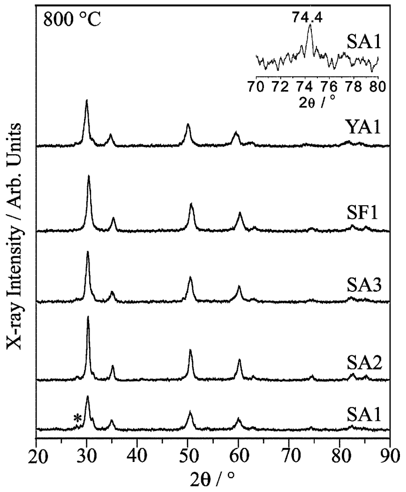

Fig. 3 XRD patterns of the oxide powders of **SA1**, **SA2**, **SA3**, **SF1** and **YA1** calcined at 800 °C (* monoclinic).

Figs. 4 and 5 give N_2 adsorption/desorption isotherms and the pore size distributions, respectively, of **SA1** and **SF1**

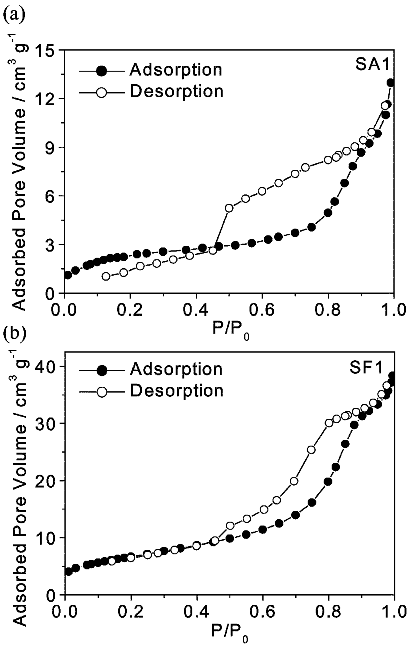

Fig. 4 N_2 adsorption/desorption isotherms of the oxide powders of **SA1** (a) and **SF1** (b) calcined at 800 °C.

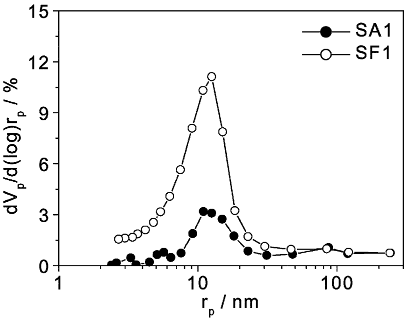

Fig. 5 Pore size distributions of the oxide powders of **SA1** and **SF1** calcined at 800 °C.

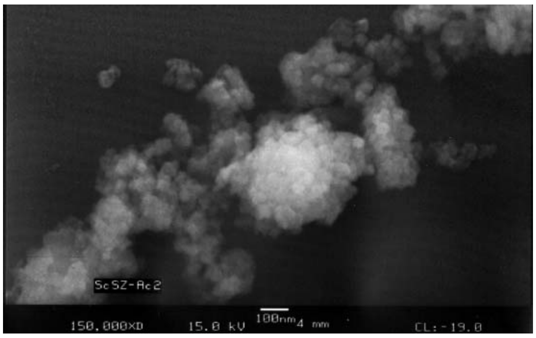

Fig. 6 SEM micrograph of the oxide powders of **SA1** calcined at 800 °C.

samples calcined at 800 °C. The shape of the isotherm is clarified into Type IV, which is characteristic of porous solids having pore widths ranging from tens to hundreds of Ångstroms.[30,31] Therefore, the gel-calcined powders are composed of an assembly of particles with large open packing. The hysteresis loop of the isotherm in the P/P_0 range of 0.5–0.9 belongs to the H3 type, and is always observed with aggregates of plate-like particles giving rise to slit-shaped pores.[31] From Fig. 5, the BJH pore diameters of **SA1** and **SF1** are determined as 10.1 and 9.0 nm, respectively. The BJH pore volumes of **SA1** and **SF1** are 0.0215 and 0.0602 cm^3 g^{-1}, respectively. Such pore sizes and volumes are suggestive of a mesoporous structure for the calcined powders.[31] Fig. 6 exhibits a typical SEM micrograph of the **SA1** powders. Even the plate-like particles with a size of *ca.* 20 nm are intra-aggregated in lumps for minimizing the total surface or interfacial energy of the system, and they display a fairly good size uniformity. Obviously, the morphological observation verifies the analyses of XRD and pore size distribution.

The BET specific surface area, BJH pore volume and pore diameter, and average grain size are summarized in Table 2. It can be noticed that nanoparticles with mesoporous structure are built after calcining at 800 °C, regardless of the polymer precursor compositions. However, the S_{BET} values of the powders derived from formic acid-containing gel are nearly three times of those derived from acetic acid-containing gel.

Sintering behavior

Fig. 7 describes the typical XRD patterns of **SA2**, **SF1** and **YA1** specimens sintered over 1000–1400 °C. The **SA2** specimen fully crystallizes in the pure cubic phase above 1200 °C. However, the **SF1** specimens achieve good-crystallization in a pure cubic structure at a low sintering temperature not exceeding 1000 °C, which is about 600–800 °C lower than the crystallization temperature in the case of using solid state reactions.[11] It is also found that the sintering temperature for **YA1** to crystallize in the pure cubic phase is about 400 °C lower than that for **SA2**, owing to the fact that yttria is much more easily doped into zirconia than scandia.

In addition, XRD studies reveal that good-crystallization in the pure cubic phase at low sintering temperatures is readily realized for the specimen prepared from the gel with a lower molar ratio of PEG to acetic acid. As the molar ratio of PEG to acetic acid in the gel is increased, the as-sintered specimens always appear polyphasic, involving cubic, tetragonal and monoclinic phases over 1000–1200 °C, even if the pre-sintered powders are in a pure or predominately cubic phase owing to the crystallite size effect. It is concluded that enhancing the acidity and coordination throughout the resulting gel, *viz.* using formic acid instead of acetic acid or decreasing the molar ratio of PEG to acetic acid, assists in improving the chemical homogeneity of the gel and thus the sinterability of the green body.

Table 2 BET specific surface area S_{BET}, BJH pore volume V_{p} and pore diameter r_{p}, and average grain size D of the gel-calcined oxide powders at 800 °C

Sample	S_{BET}/m^2 g^{-1}	V_{p}/ cm^3 g^{-1}	r_{p}/nm	D/nm
SA1	8.71	0.0215	10.1	14.4
SA2	7.57	0.0201	10.5	19.9
SA3	7.91	0.0207	10.5	14.2
SF1	24.2	0.0602	9.0	14.6
SF2	24.8	0.0826	13.6	20.8

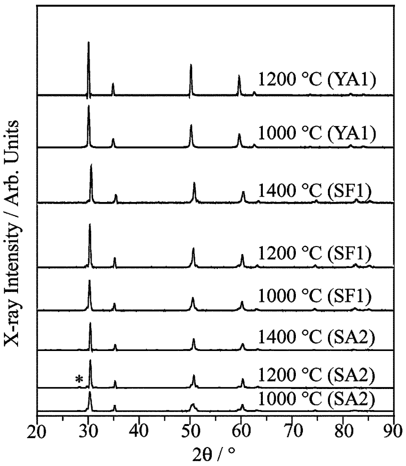

Fig. 7 XRD patterns of **SA2**, **SF1** and **YA1** specimens sintered over 1000–1400 °C (* monoclinic).

Fig. 8 gives the cross-section SEM micrographs of the **SF1** specimen sintered over 1000–1400 °C, and that of the **SA2** specimen at 1400 °C. It can be seen that dense specimens with grains of good size uniformity are yielded, on account of the chemical homogeneity on the molecular level in the precursors. For the **SF1** sample, the grains grow from about 100 nm [at 1000 °C, Fig. 8(a)] to 500 nm [at 1200 °C, Fig. 8(b)], and finally reaching a size of 1 μm [at 1400 °C, Fig. 8(c)]. The average grain size of the **SA2** sample is about 1.5 μm [at 1400 °C, Fig. 8(d)].

In the case of low densities, the sintered density could not be measured by the water immersion technique owing to the fact that water can enter the pores in the sintered body.[32] Therefore, the sintered density of the as-prepared specimen was estimated from the mass and geometric dimensions of the pellets. The ratio of the sintered density to that of the theoretical density for the **SF1** sample increased from 63% at 1000 °C, to 67% at 1200 °C and to 75% at 1400 °C. The sintered density was not very high because of the low pelletization pressure and the pore structures of the calcined nanoparticulate powders.

Lattice parameter, *a*, values of the samples sintered at various temperatures are listed in Table 3. The *a* values of $(\mathrm{ZrO_2})_{0.85}(\mathrm{REO}_{0.15})_{0.15}$ (RE = Sc, Y) are *ca.* 5.09 and 5.14 Å, respectively, which agree well with the data previously reported.[11,33] Table 3 also indicates that the *a* value of the Sc-doped sample is smaller than that of Y-doped specimen at a given temperature. Consequently, the *a* values of the as-prepared specimens are independent of the polymer precursor compositions and sintering temperatures, but do rely on the variety of the dopants.

Electrical properties

By the AC two-probe complex impedance method, two well-separated semicircles corresponding to the bulk and grain boundary conductivities, respectively, were obtained from Cole–Cole plots over the temperature range 410–650 °C. Fig. 9 is the Arrhenius plot of bulk ionic conductivity for **SF1** and **YA1** specimens sintered over 1000–1400 °C, and that for **SA1**,

(a) 1000 °C (SF1)

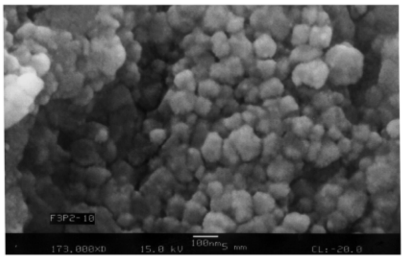

(b) 1200 °C (SF1)

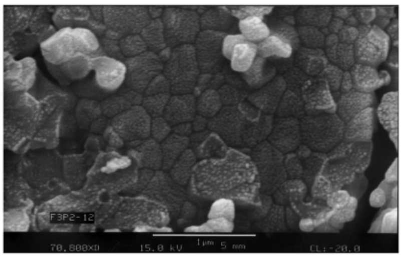

(c) 1400 °C (SF1)

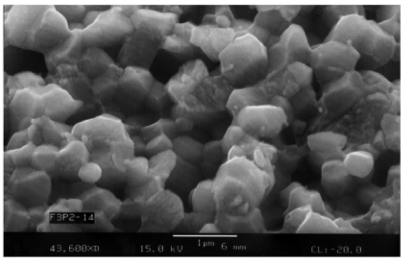

(d) 1400 °C (SA2)

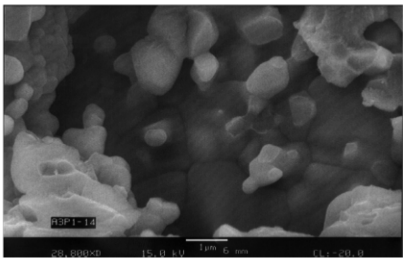

Fig. 8 Cross-section SEM micrograph of the **SF1** specimen sintered at 1000 °C (a), 1200 °C (b) and 1400 °C (c), and that of the **SA2** specimen sintered at 1400 °C (d).

SA2, **SA3**, **SF1** and **SF2** at 1400 °C. From Fig. 9(a), it is noted that the bulk σ_b for the **SF1** sample increases with increasing the sintering temperature/density from 1000 to 1400 °C, as was also observed for the $(ZrO_2)_{0.85}(YO_{1.5})_{0.15}$ polycrystalline sample by Gibson *et al.*[32] It was also reported that lower sintered densities could not only decrease the bulk conductivity, but also the grain boundary conductivity.[32] Okubo and Nagamoto found that the presence of pores in the sintered body could impair the conduction path between grains, and thus reduce the conductivity.[34]

The value of σ_b for the **SF1** sample sintered at 1200 °C is higher than that for the **YA1** sample. This keeps in line with the determined order of ionic conductivity for the rare earth-stabilized zirconia.[11] The near superposition of the fitted straight lines in Fig. 9(b) means that the polymer precursor composition does not change the bulk ionic conductivity of the specimens.

Fig. 10 depicts the Arrhenius plot of grain boundary conductivity for **SF1** and **YA1** specimens sintered over 1000–1400 °C, and that for **SA1**, **SA2**, **SA3**, **SF1** and **SF2** at 1400 °C. Values of σ_{gb} for the **SF1** sample increase with increasing sintering temperature from 1000 to 1400 °C; however, σ_{gb} for the **SF1** sample sintered at 1200 °C is a bit lower than that for the **YA1** sample [Fig. 10(a)]. Fig. 10(b) shows that the polymer precursor compositions obviously affect the grain boundary conductivity of the as-prepared specimens, because σ_{gb} is mainly determined by factors such as

Table 3 Lattice parameter *a* values of the samples after treatment at various temperatures

	a/Å			
Sample	800 °C	1000 °C	1200 °C	1400 °C
SA2	5.091(5)	5.097(2)	5.092(3)	5.092(4)
SF1	5.088(2)	5.088(2)	5.088(2)	5.075(2)
YA1	5.146(2)	5.140(2)	5.144(1)	

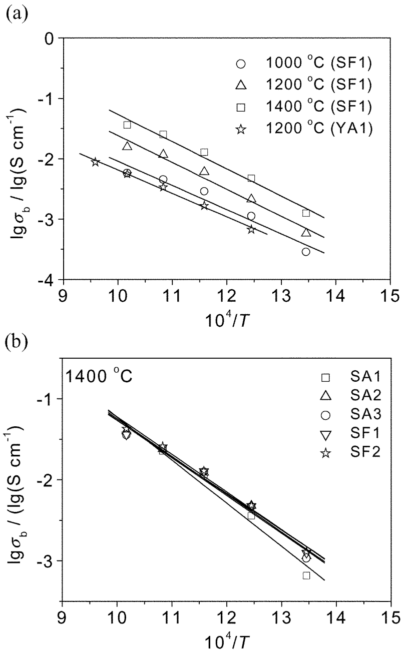

Fig. 9 Arrhenius plot of $\log\sigma_b$ *vs.* $1/T$ for **SF1** and **YA1** specimens sintered over 1000–1400 °C (a), and that for **SA1**, **SA2**, **SA3**, **SF1** and **SF2** sintered at 1400 °C (b).

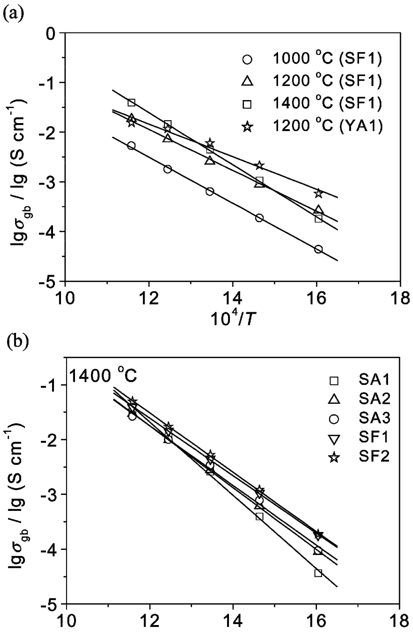

Fig. 10 Arrhenius plot of $\log\sigma_{gb}$ *vs.* $1/T$ for **SF1** and **YA1** specimens sintered over 1000–1400 °C (a), and that for **SA1**, **SA2**, **SA3**, **SF1** and **SF2** sintered at 1400 °C (b).

Table 4 Activation energies for bulk (b) and grain boundary (gb) conductivities of the samples at various sintering temperatures

	$E_a \pm 5$/kJ mol^{-1}					
	1000 °C		1200 °C		1400 °C	
Sample	b	gb	b	gb	b	gb
SA1					102	128
SA2					90	108
SA3					88	104
SF1	77	89	86	123	87	104
SF2					89	104
YA1			74	86		
8ScZr (Ref. 9)					89	97

the porosity of the sintered body and impurities segregating to the grain boundaries.[32,35]

The conductivity activation energies are given in Table 4. The determined activation energies for the bulk conductivity of **SA2**, **SA3**, **SF1** and **SF2** are very close to that determined for the Sc-doped polycrystalline (8ScZr) prepared by the coprecipitation method,[9] but are lower than that of 130–140 kJ mol^{-1} reported by Badwal over the temperature range of 400–550 °C.[36] On the other hand, the activation energies for the bulk are smaller than that for the grain boundary. Such a difference is a common phenomenon found for the electrical properties of the ceramic electrolytes.

Conclusions

$(ZrO_2)_{0.85}(REO_{1.5})_{0.15}$ (RE = Sc, Y) solid solutions in a pure cubic fluorite structure with uniform grain sizes ranging from nanometers to microns have been prepared by a Pechini-type sol–gel method, using weakly cross-linked polymers. This method adopted metal nitrates, PEG and acetic acid (or formic acid) to construct the homogeneous polymer precursor solution on the molecular level *via* coordination bond and intermolecular interactions; hence, it is a low cost, high simplicity, low-temperature synthesis. Owing to its stronger acidity and coordinating capability, formic acid seems more effective in preventing the metal hydroxides from segregating from the precursor solutions than does acetic acid during the gel formation. The Sc-doped zirconia derived from the formic acid-containing gel can achieve good-crystallization in the pure cubic phase at sintering temperatures as low as 1000 °C. The gel-calcined powders at 800 °C are mesoporous nanoparticles with narrow size distribution, and show a cubic structure attributed to the crystallite size effect. The polymeric precursor compositions display a considerable impact upon the gel formation, powder reactivity, crystallization of the sintered body, and finally the ionic conductivity of the grain boundary. However, the bulk ionic conductivity is dependent upon the sintering temperature and variety of the dopants, rather than on the precursor compositions. Both the bulk and grain boundary conductivities increase with elevating the sintering temperature/density.

Acknowledgements

Grants-in-aid from MOST (G1998061300), NSFC (Nos. 20171003, 29832010 and 20023005) and Founder Foundation of Peking University are gratefully acknowledged.

References

1 D. Segal, *J. Mater. Chem.*, 1997, **7**, 1297.
2 R. J. Bell, G. J. Millar and J. Drennan, *Solid State Ionics*, 2000, **131**, 211.
3 R. S. Torrens, N. M. Sammes and G. A. Tompsett, *Solid State Ionics*, 1998, **111**, 9.
4 S. P. S. Badwal, F. T. Ciacchi and D. Milosevic, *Solid State Ionics*, 2000, **136–137**, 91.
5 A. Brune, M. Lajavardi, D. Fisler and J. B. Wagner Jr, *Solid State Ionics*, 1998, **106**, 89.
6 H. Yamamura, N. Utsunomiya, T. Mori and T. Atake, *Solid State Ionics*, 1998, **107**, 185.
7 H. L. Tuller, *Solid State Ionics*, 2000, **131**, 143.
8 I. Kosacki, T. Suzuki, V. Petrovsky and H. U. Anderson, *Solid State Ionics*, 2000, **136–137**, 1225.
9 Y. W. Zhang, Y. Yang, S. Jin, S. J. Tian, G. B. Li, J. T. Jia, C. S. Liao and C. H. Yan, *Chem. Mater.*, 2001, **13**, 372.
10 Y. W. Zhang, S. Jin, Y. Yang, G. B. Li, S. J. Tian, J. T. Jia, C. S. Liao and C. H. Yan, *Appl. Phys. Lett.*, 2000, **77**, 3409.
11 D. W. Strickler and W. G. Carlson, *J. Am. Ceram. Soc.*, 1965, **48**, 286.
12 S. P. S. Badwal, F. T. Ciacchi, S. Rajendran and J. Drennan, *Solid State Ionics*, 1998, **109**, 167.
13 Y. W. Zhang, J. T. Jia, C. S. Liao and C. H. Yan, *J. Mater. Chem.*, 2000, **10**, 2137.
14 O. Yokota, M. Yashima, M. Kakihana, A. Shimofuku and M. Yoshimura, *J. Am. Ceram. Soc.*, 1999, **82**, 1333.
15 Y. Mizutani, M. Tamura and M. Kawai, *Solid State Ionics*, 1994, **72**, 271.
16 M. Kakihana and M. Yoshimura, *Bull. Chem. Soc. Jpn.*, 1999, **72**, 1427.
17 J. I. Langford, *J. Appl. Crystallogr.*, 1971, **4**, 259.
18 J. I. Langford, *J. Appl. Crystallogr.*, 1973, **6**, 190.
19 A. Guinier, in *Theorie et Technique de la Radiocristallographie*, Dunod, Paris, 3rd edn., 1964, p. 482.
20 E. P. Barrett, L. G. Joyner and P. H. Halenda, *J. Am. Chem. Soc.*, 1951, **73**, 373.
21 J. E. Bauerle, *J. Phys. Chem. Solids*, 1969, **30**, 2657.
22 F. Pancrazi, J. Phalippou, F. Sorrentino and J. Zarzycki, *J. Non-Cryst. Solids*, 1984, **63**, 81.
23 A. C. Geiculescu and H. G. Spencer, *J. Sol–Gel Sci. Technol.*, 1999, **14**, 257.
24 S. W. Kwon, S. B. Park, G. Seo and S. T. Hwang, *J. Nucl. Mater.*, 1998, **257**, 172.
25 K. Q. Huang and J. B. Goodenough, *J. Solid State Chem.*, 1998, **136**, 274.
26 M. Yashima, T. Kato, M. Kakihana, M. A. Gulgun, Y. Matsuo and M. Yoshimura, *J. Mater. Res.*, 1997, **12**, 2575.
27 M. Yashima, K. Ohtake, M. Kakihana and M. Yoshimura, *J. Am. Ceram. Soc.*, 1994, **77**, 2773.
28 R. C. Garvie, *J. Phys. Chem.*, 1965, **69**, 1238.
29 J. S. Lee, T. Matsubara, T. Sei and T. Tsuchiya, *J. Mater. Sci.*, 1997, **32**, 5249.
30 S. J. Gregg, *Colloids Surf., A*, 1986, **21**, 109.
31 K. S. W. Sing, D. H. Everett, R. A. W. Haul, L. Moscou, R. A. Pierotti, J. Rouquerol and T. Siemieniewska, *Pure Appl. Chem.*, 1985, **57**, 603.
32 I. R. Gibson, G. P. Dransfield and J. T. S. Irvine, *J. Mater. Sci.*, 1998, **33**, 4297.
33 H. G. Scott, *J. Mater. Sci.*, 1975, **10**, 1527.
34 T. Okubo and H. Nagamoto, *J. Mater. Sci.*, 1995, **30**, 749.
35 M. Aoki, Y.-M. Chiang, I. Kosacki, L. J.-R. Lee, H. L. Tuller and Y. P. Liu, *J. Am. Ceram. Soc.*, 1996, **79**, 1169.
36 S. P. S. Badwal, *J. Mater. Sci.*, 1983, **18**, 3117.